# Wavelet analysis of turbulent structures in a magnetized pure electron plasma

Y. Kawai* and Y. Kiwamoto
*Graduate School of Human and Environmental Studies, Kyoto University, Yoshida Nihonmatsu-cho, Sakyo-ku, Kyoto 606-8501, Japan*
(Received 25 April 2008; published 4 September 2008)

Wavelet analysis is applied to examine two-dimensional (2D) structures of pure electron plasma density distribution observed in a free-decaying turbulent stage starting from an unstable distribution. In contrast to the traditional Fourier analysis, the simultaneous resolution of the structures in terms of the physical coordinates and length scales (or wave numbers) allows us to discriminate instrumental dot noises without generating spurious high wave-number components that tend to distort the energy and enstrophy spectra. With this analysis at each time segment, the following features are clearly observed: Intermittency in the structures of electron density distribution, that is equivalent to the 2D vorticity distribution, is clearly demonstrated in terms of the scale-resolved kurtosis. The upward cascade of the enstrophy in the wave-number space is associated with the development of vortex filamentation in the physical space. Controlled discrimination of the coherent component in terms of the wavelet coefficients of the observed density distribution indicates significant contribution of persisting coherent vortices in steepening the energy spectra of the 2D turbulence far above the theoretically predicted power law of $k^{-3}$.

DOI: 10.1103/PhysRevE.78.036401 PACS number(s): 52.27.Jt, 47.27.Jv

## I. INTRODUCTION

Macroscopic dynamics of pure electron plasmas transverse to a strong magnetic field $B_0$ are equivalent to two-dimensional (2D) vortex dynamics of inviscid and incompressible fluids, through the relation $\zeta = en/\varepsilon_0 B_0$ between the vorticity $\zeta$ and the electron density $n$ [1]. Here, $-e$ and $\varepsilon_0$ are the electron charge and the dielectric constant in vacuum, respectively. By taking advantage of this equivalence, fundamental processes in 2D turbulence have been examined extensively by employing magnetized pure electron plasmas which evolve from unstable initial distributions into a stable metaequilibrium state via stochastic dynamics of vortex patches [1–7].

Extensive analyses of fine structures in the density distribution based on the Fourier expansion have revealed that the spectral dynamics of the energy and enstrophy in the wave-number space are qualitatively consistent with the theoretical description of the 2D turbulence [8–10], i.e., the energy is transferred to larger scales and the enstropy cascades toward smaller scales at a constant transfer rate [7]. However, there remains uncertainty in understanding how this spectral dynamics are connected to the vortex dynamics in the physical space. This uncertainty is to be attributed to the inherent nature of the Fourier transform that loses information of the location of vortex structures.

In order to resolve this difficulty, wavelet analyses have been employed since the end of the 1980's for the local analysis of turbulent flows observed in experimental and numerical studies [11]. Spatially localized wave packets, called wavelets, allow us to analyze turbulent fields in terms of both coordinates (physical space) and scale (wave-number space) simultaneously within the limits of the uncertainty principle.

In this paper, the orthogonal wavelet decomposition is applied to the experimentally observed density distributions which were previously investigated in terms of Fourier analysis [7]. The spectral dynamics in the wave-number space are examined in relation to the vortex dynamics in the physical space to clarify characteristic features in 2D turbulence from a physical point of view.

The outline of this paper is as follows: First, we introduce the analyzing wavelet used in this paper in Sec. II A, and then in Sec. II C, resorting to the wavelet-based noise extraction method, we remove instrumental noises from the raw data of observed density distribution and evaluate the effects of the noises to the data analyses reported in previous papers. In Sec. III, on the basis of the denoised data, we investigate the various properties of the turbulent structures with the wavelet decomposition introduced in Sec. III A. In Sec. III B, physical dynamics of the density structure are examined at each length scale, and in Sec. III C, statistical quantities are evaluated from the wavelet coefficients. In Sec. III D, we focus our examination onto the contribution of coherent vortex structures to the spectra that characterize the 2D turbulent system as a whole. The conclusion is given in Sec. IV.

## II. REDUCTION OF DENOISED DISTRIBUTION

### A. Introduction of wavelets

The analyzing wavelets need to be selected in terms of compact support, symmetry, smoothness, number of vanishing moments, and calculation efficiency [11,12]. In the following analysis, we employ the Coiflet order 12 wavelet which is compactly supported, quasisymmetric, and has four vanishing moments [13]. Because the electrons are confined in the conducting wall in the experiment, the approximation of periodicity may cause deformations in the energy spectra in the low wave-number range. Nevertheless, as far as we have examined the spectra in the range high above the low wave number, the spectral structures are confirmed to be

*kwaiyosuke@h01a0395.mbox.media.kyoto-u.ac.jp

 ©2008 The American Physical Society

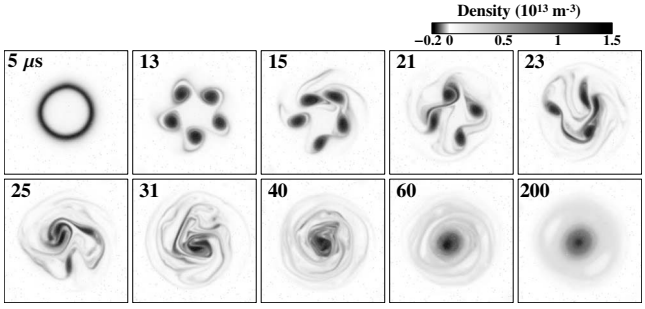


FIG. 1. Images of the time evolution of the density distribution. Each image is denoised using the procedure described in Sec. II C. The time of observation (in $\mu$s) is indicated at the upper left corner.

consistent with previous results that were obtained with Fourier analysis on the experimental geometry [7].

### B. Experimental scheme

The experiment was carried out using a pure electron plasma confined in a Penning-Malmberg trap consisting of a uniform magnetic field ($B_0$=0.048 T) and a square-well potential, which is in the same configuration as previously reported [5–7,14,15]. The vortex dynamics start with a spontaneous formation of density patches via a nonlinear stage of the diocotron instability of a ring-shaped density distribution [4,6,7]. Through successive mergers between the patches, accompanied by a generation of filamentary structures, the turbulent state relaxes into a stable density distribution of a single-peaked profile. Details of the experimental configuration and diagnostic methods have been reported in Ref. [5–7,14–16]. The time evolution of the 2D density distribution was observed destructively by extracting all electrons along the magnetic field lines, accelerating them onto a phosphor screen and digitizing the resultant luminosity distribution with a charge-coupled-device (CCD) camera at each time step of the relaxation. The observed evolution taken from one of the data sets is shown in Fig. 1. Each image is denoised in a different way from the previous paper [7].

### C. Extraction of instrumental noises

The denoising procedure is shown in Fig. 2 by taking one of the snap shots before denoising as an example. The left panel represents the raw data of 2D density distribution $n_0(x,y)$ observed at $t$=31 $\mu$s in Fig. 1. Randomly distributed dots are visible around the spiraling vortices. The low-level dots with stochastic distribution are associated with the randomly accumulated charge on the pixels of CCD due to dark current. If we subtract the height of the dots uniformly from the raw data, discontinuities appear around the vortices to cause spuriously components at high wave numbers in Fourier spectra. In this section, we examine the contribution of the instrumental noise to physical analysis by applying the wavelet-based noise extraction method to the raw data of density distribution.

The probability density function (PDF) of $n_0(x,y)$ in the left panel is plotted in the right panel in Fig. 2 with the solid curve. The PDF in the region of $n<0$ fits to a Gaussian

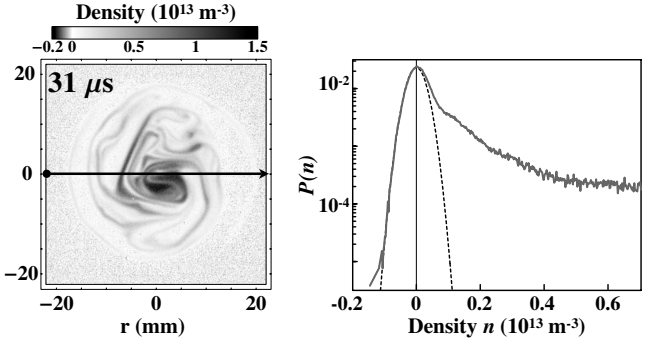


FIG. 2. An example of the raw data of electron density distribution $n_0(x,y)$ (left) and its probability density function (PDF) $P(n)$ (right). The dashed curve is the Gaussian fit to $P(n)$ optimized in the negative region of the electron density $n$.

distribution represented by a dashed curve. Since the density $n$ cannot be negative, this part of $P(n)$ should belong to the instrumental noise. In order to extract the Gaussian component systematically, we apply a denoising procedure to $n_0(x,y)$ in Fig. 2, which consists of decomposing the 2D image of $n_0(x,y)$ into a wavelet series and reconstructing the next-step distribution from the coefficients whose moduli are larger than the threshold value $\sigma\sqrt{\ln N}$ [17,18]. Here, $N$ is the total pixel number $512\times512$, and $\sigma$ is the variance of the noise that represents the Gaussian distribution fitting to the PDF with $n<0$. The distribution denoised in this manner is plotted in the $t$=31 $\mu$s frame of Fig. 1.

Some details of the denoising procedure are given in Fig. 3(a) as 1D profiles along the chord $y$=0 [indicated by the arrow in the left panel of Fig. 2(a)]. Here, the raw data of the density distribution (gray line) and the denoised distribution (solid line) are shown together in the upper part, and the difference of the two distributions (dashed line) is plotted in the lower part. The latter represents the noise extracted from the wavelet series of the raw data. The PDF for each distribution in 2D space is plotted in Fig. 3(b) in the form normalized at $n$=0. The dashed line representing the PDF of the noise component is confirmed to be very close to the Gaussian distribution. The PDF of the denoised distribution in the range $n<0$ is reduced substantially, indicating that most of the unphysically negative part of the raw data has been removed.

The energy spectra associated with the separated distributions are plotted in Fig. 3(c). The spectrum of the instrumental noise (dashed line) shows the power-law scaling $E(k)$ $\propto k^{-1}$ in the wave-number domain of $k\geqslant1000$. Since the energy spectrum is defined as $E(k)=\frac{1}{2}\int_0^{2\pi}kd\varphi|e\hat{n}(\mathbf{k})/\varepsilon_0B_0|^2k^{-2}$ [where $\hat{n}(\mathbf{k})$ and $\varphi$ are the Fourier transform of the density distribution and the azimuthal angle of $\mathbf{k}$, respectively], this profile means $|\hat{n}(\mathbf{k})|\approx$const, so that the extracted noise is uniformly distributed over the spectral space as a white (uncorrelated) noise. This also means that the instrumental noise cannot be removed with simple low-pass Fourier filtering.

In Fig. 3(c), it is also noticeable that the spectrum of the noise exceeds that of the denoised distribution in amplitude at high wave numbers $k\geqslant7500$. This implies that physical quantities evaluated from the raw data, particularly those characterizing the fine scale structures, can be substantially

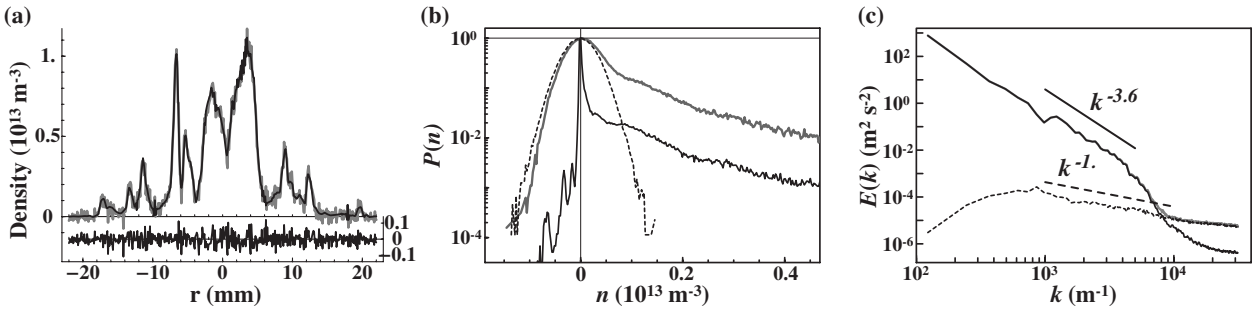


FIG. 3. Extraction of instrumental noises. (a) Density distributions along the chord $y=0$ in the left panel of Fig. 2 consisting of raw data (gray lines), denoised (solid lines), and extracted noise (dashed lines) distributions (the noise is scaled along the vertical axis to the right). (b) PDF of each component in 2D space. (c) Energy spectrum for each distribution.

influenced by the instrumental noise. To evaluate the contribution of the instrumental noise, we calculate the integral quantities, the enstrophy $Z_2=\frac{1}{2}\int d\mathbf{r}^2(en/\varepsilon_0 B_0)^2$ and the palinstrophy $\frac{1}{2}(e/\varepsilon_0 B_0)^2\int d\mathbf{r}^2|\nabla n|^2$, for the raw denoised and noise distributions, and plot as a function of time in Fig. 4. The palinstrophy is a measure of the fineness in the spatial structures. Throughout the whole process, the gray and closed squares overlap, indicating that more than 95% of the enstrophy of the raw data is retained in the denoised distribution, while 70–95% of the palinstrophy in the raw data is found to belong to the instrumental noise.

On the basis of the denoised distribution, we reevaluated the effective viscosity coefficient $\nu=-(1/2P)DZ_2/Dt$, which is a measure of the degree of enstrophy dissipation [7–10]. The time evolution of the experimentally determined viscosity is plotted in Fig. 5, together with the theoretically predicted coefficient $\nu_{th}$. The latter is estimated by introducing the parameters of the present experiment [the electron density $n(r)\leqslant 10^{13}$ m$^{-3}$, the axial length $L(r)\sim 0.08$ m and the temperature $\sim 0.3$ eV, etc.] into the proposed formula [19]. The effective viscosity $\nu$ has increased by a factor of 4 from the previously published value [7] as a result of the reduction of instrumental noises in the palinstrophy, though it still agrees with $\nu_{th}$ within a factor of 2. Moreover the two viscosities show quite similar variations over the whole time of the relaxation, which were not clearly observed in the previous report. As stated in Ref. [7], this agreement may suggest that the stochastic motions of individual particles under fluctuating fields play a important role in the dissipation process of vortex dynamics, and the discrepancy in the absolute value may be attributed to the theoretical assumption that viscous transport proceeds in a cylindrically symmetric configuration under stationary state.

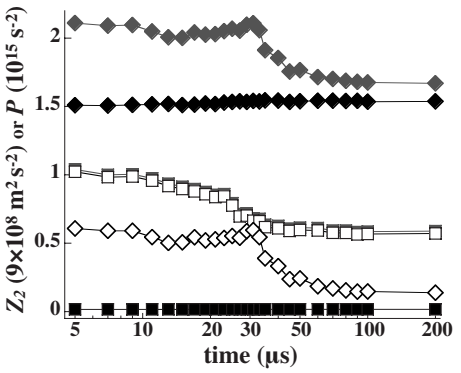


FIG. 4. Time evolution of the enstrophy $Z_2$ (squares) and palinstrophy $P$ (diamonds) evaluated from the 2D density distribution of raw data $n_0(x,y)$ (gray symbols), denoised distribution (open symbols), and noise distribution (closed symbols).

## III. WAVELET ANALYSIS OF TURBULENT STRUCTURE

### A. Multiresolution analysis of density distribution

In this section, we analyze the structures of the turbulent electron plasma in terms of both coordinates and scale on the basis of the wavelet coefficients obtained from the denoised density distribution $n(x,y)$. The distribution is decomposed into an orthogonal wavelet series from the smallest scale $2^{-(J-1)}$ (where $J=\log_2\sqrt{\mathrm{N}}=9$) to the largest scale $2^0$ using a two-dimensional multiresolution analysis [11,13,18] given as

$$n(x,y)=\tilde{n}^0_{0,0}\phi^0_{0,0}(x,y)+\sum_{j=0}^{J-1}\sum_{i_x=0}^{2^j-1}\sum_{i_y=0}^{2^j-1}\sum_{\mu=1}^{3}\tilde{n}^{\mu,j}_{i_x,i_y}\psi^{\mu,j}_{i_x,i_y}(x,y),$$

$$\phi^j_{i_x,i_y}(x,y)=\phi^j_{i_x}(x)\phi^j_{i_y}(y),\quad \psi^{1,j}_{i_x,i_y}(x,y)=\phi^j_{i_x}(x)\psi^j_{i_y}(y),$$

$$\psi^{2,j}_{i_x,i_y}(x,y)=\psi^j_{i_x}(x)\phi^j_{i_y}(y),\quad \psi^{3,j}_{i_x,i_y}(x,y)=\psi^j_{i_x}(x)\psi^j_{i_y}(y),$$

where $\phi^j_{i_x}(x)$ and $\psi^j_{i_x}(x)$ are the scaling function and the corresponding wavelet, respectively. Due to the orthogonality,

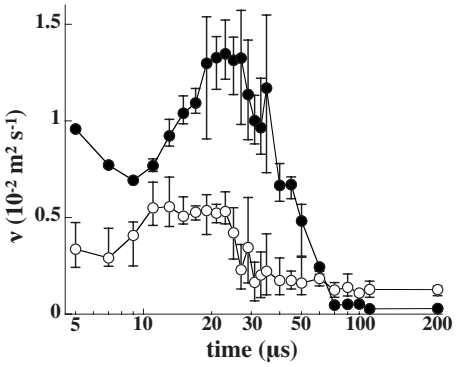


FIG. 5. Time evolution of the viscosity coefficients reevaluated from the denoised data $\nu$ (●) and calculated from the theoretical formula $\nu_{th}$ (○).

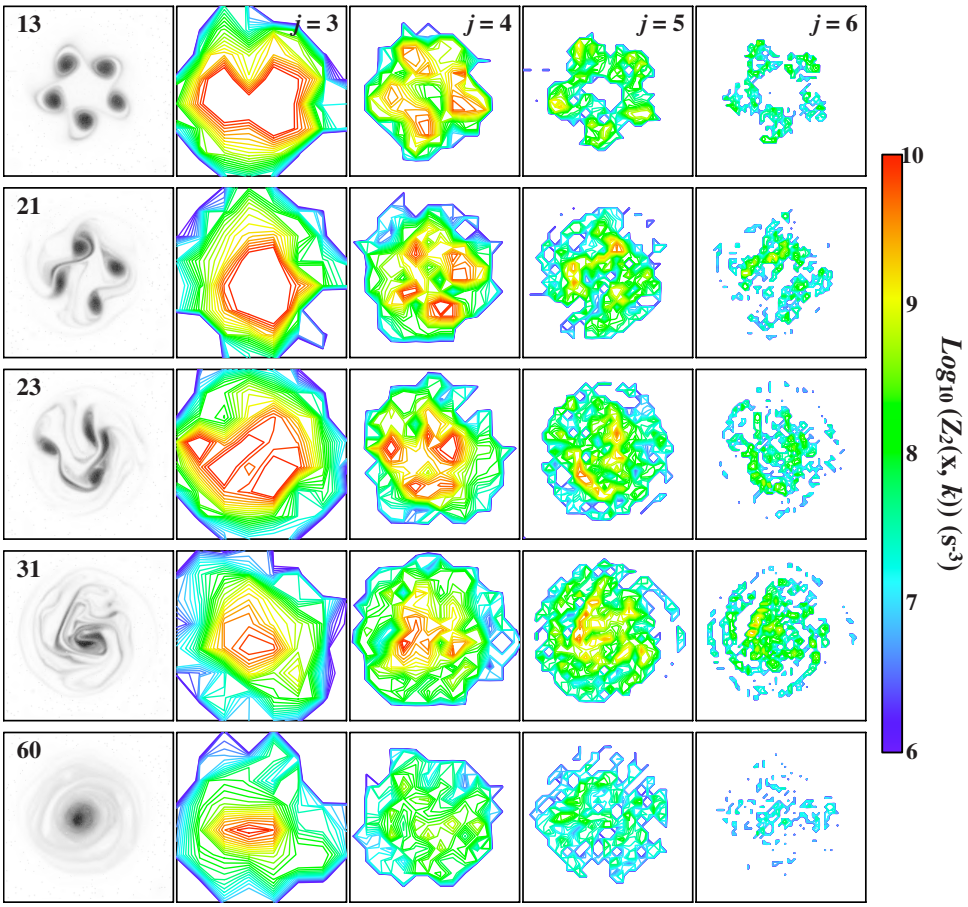


FIG. 6. (Color online) Contours of the local enstrophy spectrum $\tilde{Z}_2(\mathbf{x},k_j)$ for scales $j=3-6$ corresponding to the density distributions at each time step (left panels).

the wavelet coefficient $\tilde{n}^{\mu,j}_{i_x,i_y}$ at scale $2^{-j}$ and position $(i_x,i_y)$ is given by $\tilde{n}^{\mu,j}_{i_x,i_y}=\langle n,\psi^{\mu,j}_{i_x,i_y}\rangle=\int n(\mathbf{r})\psi^{\mu,j}_{i_x,i_y}(\mathbf{r})d\mathbf{r}$, and $\tilde{n}^0_{0,0}=\langle n,\phi^0_{0,0}\rangle$ corresponds to the mean value of the density.

In the actual analyses, the above expansion is applied to the raw data $n_0(x,y)$ and the denoised distribution $n(x,y)$ is subject to further analyses with decreased number of coefficients. Unless otherwise noted, the results presented in the following sections are all obtained from the denoised density distribution observed at $t=31$ $\mu$s.

### B. Dynamics of enstrophy distribution

First, we examine the spatial distribution of the density structure at each length scale in terms of the local enstrophy spectrum $\tilde{Z}_2(\mathbf{x},k_j)$ of wave number $k_j=k_0 2^j$ at the position $\mathbf{x}=(i_x,i_y)2^{9-j}\Delta x$ as evaluated from the wavelet coefficients $\tilde{n}^{\mu,j}_{i_x,i_y}$ [12,20,21]

$$\tilde{Z}_2(\mathbf{x},k_j)=\frac{1}{2}\left(\frac{e}{\varepsilon_0 B_0}\right)^2\sum_{\mu=1}^{3}(\tilde{n}^{\mu,j}_{i_x,i_y})^2/A_j,$$

where

$$A_j=\Delta k_j\Delta x_j^2,$$

$$\Delta x_j=2^{9-j}\Delta x,$$

$$\Delta k_j=\sqrt{k_{j+1}k_j}-\sqrt{k_j k_{j-1}},$$

Here $\Delta x=0.1$ mm is the smallest resolvable scale on the CCD image, and $k_0$ is determined by the filtering property of the Fourier-transformed wavelet and scaling function. $\tilde{Z}_2(\mathbf{x},k_j)$ is defined as the density of the enstrophy per unit area $\Delta x_j^2$ and per unit wave-number range $\Delta k_j$, so that $\Sigma_\mu(\tilde{n}^{\mu,j}_{i_x,i_y})^2$ is divided by the factor $A_j$ [20].

The contour of the enstrophy density $\tilde{Z}_2(\mathbf{x},k_j)$ in the scale of $j=3-6$ at each time step is plotted in Fig. 6 together with the corresponding electron density distribution to the left. The vortex patches generated at $t=13$ $\mu$s are dominated by $\tilde{Z}_2(\mathbf{x},k_j)$ at $j=4$, and the coherent property of these structures, spatial locality or high vorticity, is retained throughout the merging process between the patches. In contrast, in smaller scales of $j=5-6$, $\tilde{Z}_2(\mathbf{x},k_j)$ extends spatially along with the generation of filamentary structures. At the end of the merging process at $t=31$ $\mu$s, while the filaments are most conspicuous in the scale of $j=5-6$, a single-peaked distribution forms accompanied by the sharpening of $\tilde{Z}_2(\mathbf{x},k_j)$ at $j=3$. After the formation of a single vortex, the amplitudes of $\tilde{Z}_2(\mathbf{x},k_j)$ at $j=4-6$ decrease due to the smoothing of the fine-scale structures, and finally a bell-shaped core distribution with the characteristic scale of $j=3$ forms surrounded by a low-density halo. The distributions of $\tilde{Z}_2(\mathbf{x},k_j)$ at scales $j=7-8$ (not shown in Fig. 6) are masked by remaining noise component.

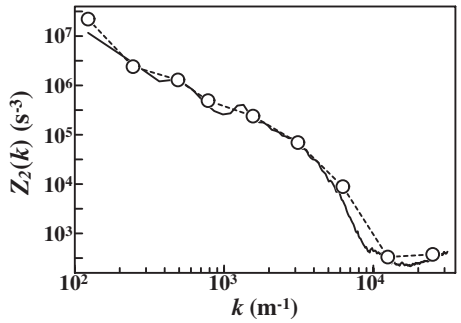


FIG. 7. Enstrophy spectra obtained from the wavelet coefficients (○+dashed line) and Fourier coefficients (solid line) at $t=31$ $\mu$s.

The wavelet-based enstrophy spectrum in the wavenumber space is obtained by summing $\tilde{Z}_2(\mathbf{x},k_j)$ over all positions, as $\tilde{Z}_2(k_j)=\Sigma_{i_x,i_y}\tilde{Z}_2(\mathbf{x},k_j)\Delta x_j^2$. It is plotted in Fig. 7 with open circles, together with the Fourier-based spectrum $Z_2(k)$ with solid line. As observed in Fig. 7, $\tilde{Z}_2(k_j)$ agrees quite well with $Z_2(k)$. The scales $j=3-6$ in the wavelet representation correspond to the inertial range in the wavenumber space, where the enstrophy transfer rate remains almost constant at a finite value as confirmed in the previous paper [7]. The agreement between $\tilde{Z}_2(k_j)$ and $Z_2(k)$, if combined with Fig. 6 that describes the spatial dynamics at each length scale, indicates that the enstrophy cascade proceeds involving a wide range of length scales extending from vortex patches to fine filamentary structures.

### C. Characteristic features of turbulent structures

We proceed with our statistical examination of the space-time resolved data as given in Fig. 6. Figure 8 shows the scale-dependent higher-order moments evaluated from the wavelet coefficients [note that the second-order moment corresponds to the wavelet enstrophy spectrum $\tilde{Z}_2(k_j)$]. Here, the skewness $S_j$ and the kurtosis $K_j$ are evaluated at different scales from the 2D distributions of the raw $n_0(x,y)$ (□), denoised $n(x,y)$ (●), and the extracted noise (▲) distributions. The $p$th order moment at scale $j$ is defined as

$$M_{p,j}=\frac{1}{3\times 2^{2j}}\sum_{i_x,i_y=0}^{2^j-1}\sum_{\mu=1}^{3}(\tilde{n}_{i_x,i_y}^{\mu,j}-\bar{M}_j)^p,$$

where $\bar{M}_j=\Sigma_{i_x,i_y,\mu}\tilde{n}_{i_x,i_y}^{\mu,j}/(3\times 2^{2j})$ is the mean value at scale $j$. The skewness $S_j$ ($p=3$) and kurtosis $K_j$ ($p=4$) are evaluated as [21,22]

$$Q_{p,j}=\frac{M_{p,j}}{(M_{2,j})^{p/2}}.$$

With regard to the noise structure, both the skewness and kurtosis are observed to be close to the Gaussian value of $S_j\sim 3$ and $K_j\sim 0$, except at the scale of $j=0-2$ where the number of the coefficients is too small (0 at $j=0-1$ and 4 at $j=2$) to give a statistically meaningful value. At scales $j=7-8$ of the raw data $n_0(x,y)$, both $S_j$ and $K_j$ approach the Gaussian. This observation is attributed to the overwhelming

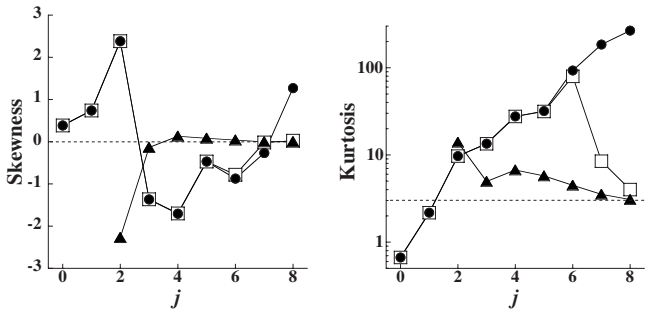


FIG. 8. Scale dependence of statistical quantities, the skewness $S_j$ (left) and kurtosis $K_j$ (right), for the raw (□), denoised (●), and noise (▲) distributions at $t=31$ $\mu$s. The horizontal dashed lines indicate the Gaussian values, $S_j=0$ and $K_j=3$.

fraction shared by the instrumental noises in the high wavenumber domain $k\geqslant 7500$ of the raw data, as noticed in Fig. 3(c). The density distribution $n(x,y)$ after denoising process shows clear characteristics that the kurtosis $K_j$ increases in the whole range of the scale index $j$, though the skewness does not shows any systematic trend. The clear trend of the kurtosis suggests that the structure of the vorticity distribution [$\propto n(x,y)$] is intermittent in the turbulent state [23].

On the basis of the above observation, we examine the time evolution of the statistical quantities, $\tilde{Z}_2(k_j)$, $S_j$, and $K_j$, separated into different length scales. The details of the analysis are described in Fig. 9. In the frame of enstrophy to the left, while $\tilde{Z}_2(k_j)$'s at $j=2-3$ decay substantially in association with the vortex merger ($13\leqslant t\leqslant 31$ $\mu$s), $\tilde{Z}_2(k_4)$ remains almost constant, but $\tilde{Z}_2(k_j)$'s at $j=5-6$ show a rapid increase and reach the maximum at $t=31$ $\mu$s. This temporal behavior is consistent with the observation in Fig. 6. The successive change of the enstrophy at each length scale supports the physical interpretation that the enstrophy cascades toward smaller scales through the filamentation process of the vortex structures.

In contrast to the enstrophy, the skewness and kurtosis show only a slight systematic change during the merger-dominant period. However, these two quantities show unambiguous changes in the generation phase of the vortex patches around $t=13$ $\mu$s, in which $S_j$ increases from negative to zero and $K_j$ decreases at the scales of $j=3-6$. $K_j$ also decreases at $t>31$ $\mu$s at the scales of $j=4-5$ along with the reduction in the enstrophies at $j=3-6$. The kurtosis at $j=3-5$ is observed to converge into almost equal value after 40 $\mu$s. This means that intermittency in the structures of density distribution disappears in association with the dissipation of the fine-scale fluctuations.

### D. Effect of coherent components on turbulent spectrum

In numerical studies of a free-decaying 2D turbulence [24–26], it has been observed that a long-time persistence of high vorticity structures tends to impede the cascade of enstrophy and causes the slope of the energy spectrum $E(k)$ $\propto k^{-\alpha}$ to be steeper than the theoretically predicted value of $\alpha=3$ [8–10]. In the experiment, the influence of the coherent

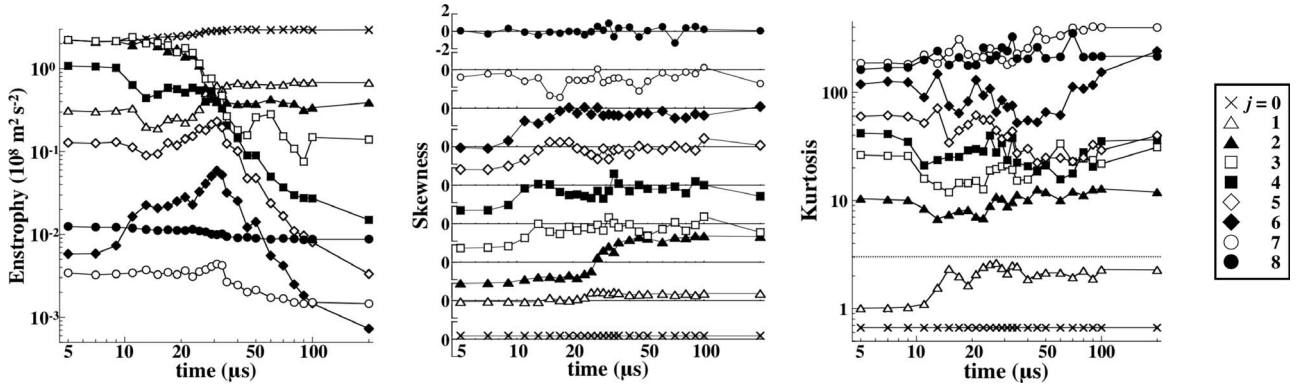


FIG. 9. Time evolution of the enstrophy (left), skewness (middle), and kurtosis (right) at each length scale $j=0$ (×), 1 (△), 2 (▲), 3 (□), 4 (■), 5 (◇), 6 (◆), 7 (○), 8 (●). Origin of the skewness is shifted at each scale for clarity.

vortices was also observed in the spectral distributions of the energy and transfer rate of the enstrophy [7]. In this section, we examine contributions of the coherent vortices to the turbulent cascade process in terms of the steepening of the energy spectrum.

Here, we employ the extraction method proposed by Kevlahan and Farge [27] to separate the denoised density distribution $n(x,y)$ into two parts, the coherent component $n_C(x,y)$ and the filamentary component $n_F(x,y)$. First, the wavelet coefficients are squared and arranged in the order of decreasing amplitude, and its cumulative sum (i.e., cumulative enstrophy) is evaluated. The result is plotted in Fig. 10. The sum is normalized to the total enstrophy ($6\times10^8$ m$^2$/s$^2$). It is found that more than 70% of the total enstrophy is shared by only 5 coefficients.

Due to the orthogonality of the wavelet functions, the denoised density distribution $n(x,y)$ can be decomposed into arbitrary subsets of distributions. If we describe as $n(x,y)=n_C(x,y)+n_F(x,y)$ separating the two components at the enstrophy fraction of 88.2% in the cumulative enstrophy (see Fig. 10), distributions of $n_C(x,y)$ and $n_F(x,y)$ are given as in Fig. 11(a). The reason for this discrimination is discussed later. The two panels demonstrate a clear contrast between the bulk distribution and highly-structured filamentary distribution. The 1D profiles of $n(x,0)$, $n_C(x,0)$, and $n_F(x,0)$ along the chord $y=0$ are plotted in Fig. 11(b). The difference in the length scale may be observed: the dominant scales composing $n_C(x,y)$ are $j=0-3$, and those composing $n_F(x,y)$ are $j=4-8$.

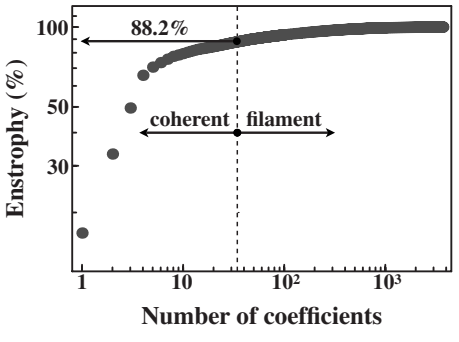


FIG. 10. Cumulative sum of the squared wavelet coefficients $(\tilde{n}^{\mu,j}_{i_x,i_y})^2$ which are ordered by amplitude. The dashed line indicates the number of the largest coefficients containing 88.2% of the total enstrophy. These coefficients compose the coherent component $n_C(x,y)$, and the remaining coefficients compose the filamentary component $n_F(x,y)$.

In Ref. [27], the threshold for the separation was determined at the point where the slope changes in the logarithmic plot of cumulative enstrophy. In Fig. 10, however, the slope changes continuously in the plot, so that the threshold is not clearly determinable. Therefore we carry out the separation with various trial values of threshold ranging from 80 to 100%, and compare the shapes of the spectra for the coherent and filamentary components. Comparison is made in Fig. 12 for the coherent (○) and filamentary (●) components in terms of the power index $\alpha$ estimated from a linear least-square fit to log-log plot of the energy spectrum $E(k)\propto k^{-\alpha}$ in the wave-number region of $700\leqslant k\leqslant 5000$.

The slope of the spectrum for the filamentary component varies continuously from the index $\alpha=3.6$ representing the

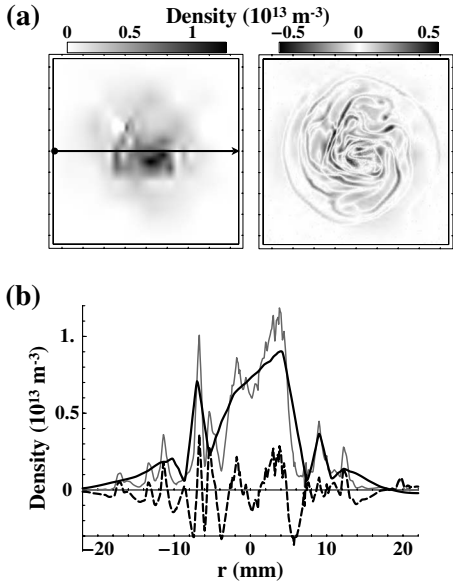


FIG. 11. (a): 2D profiles of the coherent component $n_C(x,y)$ (left) and the filamentary component $n_F(x,y)$ (right) separated at the threshold value of 88.2%. (b) 1D profiles of the denoised density distribution $n(x,0)$ (gray line), $n_C(x,0)$ (solid line), and $n_F(x,0)$ (dashed line) along the chord $y=0$.

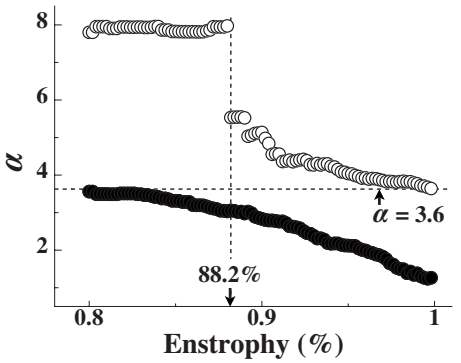


FIG. 12. Power index $\alpha$ of the energy spectrum $E(k) \propto k^{-\alpha}$ in the wave-number region of $700 \leqslant k \leqslant 5000$ is plotted for coherent (○) and filamentary (●) components as a function of the threshold value in the cumulative enstrophy. The vertical dashed line indicates the threshold value of 88.2% and the horizontal dashed line indicates the power index of the whole spectrum $\alpha=3.6$.

whole spectrum down to the index $\alpha=1$ characterizing the white noise [see Fig. 3(c)]. In contrast, the spectrum for the coherent component shows the power-law scaling when the threshold is set at a value above 88.2%, and the index decreases continuously from 5.6 down to 3.6 as the threshold increases. If the threshold is lowered below 88%, the power index $\alpha$ increases discontinuously up to 8 and remains around this value. The corresponding energy spectrum becomes increasingly oscillatory due to the reduction of the number of wavelet constituents. The observed transition in the energy spectrum of coherent component suggests that the appropriate threshold should lie around 88.2%. The distributions plotted in Fig. 11 are based on this discrimination.

Figure 13 shows the energy spectra of the coherent and filamentary components separated at the threshold value of 88.2% as plotted in Fig. 11. Each energy spectrum shows the power-law scaling with $\alpha=5.5$ for $n_C$, and $\alpha=3$ for $n_F$ over a wide domain in the wave-number space, which is consistent with the theoretically expected index [8–10]. Because the present argument for determining the threshold is not clearly based on definite criteria, there remain some ambiguities concerning to the extraction of the coherent component. For all this weakness, the extensive wavelet analysis of the experimental data clearly shows that the steepness of the energy spectrum increases with increasing fraction of the coherent component in the total structures under examination. This conclusion based on the experiment is consistent with the findings based on numerical simulations [26,27].

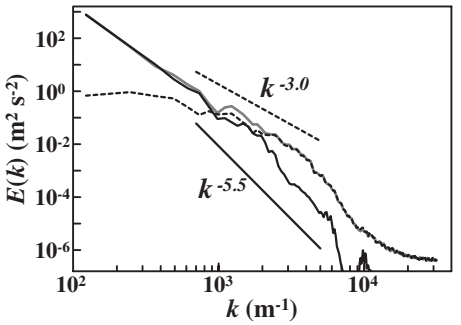


FIG. 13. The energy spectra of the total density distribution (gray line), and the coherent (solid line) and filamentary (dashed line) components separated at the threshold value of 88.2% in the cumulative enstrophy.

In closing this section, we note the theoretical arguments raised by Saffman [28] and Gillbert [29] with regard to the power index of the energy spectrum. Saffman assumed that turbulence is dominated by vorticity discontinuities (i.e., filamentary structures) generated via vortex interactions, and analytically obtained the spectral index of $k^{-4}$ for the case with isotropic and dilute distribution of discontinuities. Later, on a model with spiral structures surrounding coherent vortex patches, Gillbert argued that the accumulation of the discontinuities brings the Saffman's $k^{-4}$ spectrum down to $k^{-3}$ as derived from the cascade model [8–10]. These theoretical pictures suggest that the reduction of the spectral index representing the filamentary part, as shown in Fig. 12, corresponds to the accumulation of the filamentary structures in the Gillbert's model in the course of the reduction of coherent components relative to the filamentary components.

## IV. CONCLUSION

The objective of this paper is to explore the structural analyses of two-dimensional turbulence that appears as vortex dynamics, beyond the scope achieved so far in terms of the Fourier expansion that loses the information on the spatial coordinates of the structure under consideration. The wavelet analysis is applied to the same data set that was analyzed extensively in the previous paper [7] with the Fourier analysis, in order to clarify the advantage of holding a simultaneous resolution in the physical and wave-number spaces. We also take the advantage of the equivalence of the density distribution of a magnetized pure electron plasma to the vorticity distribution in two-dimensional fluid dynamics.

The basic achievement is the successful removal of instrumental noises that, in the previous paper, dominated the energy and enstrophy spectra in the high wave-number region. The dynamics of the denoised distribution are analyzed at different levels of length scale so that the vortex dynamics in the physical space can be related directly to the spectral transport in the wave-number space. The enstrophy cascade is shown to proceed through the filamentation process of the vortices. The scale-resolved wavelet analyses have revealed the intermittency in the structures of density distribution. The free-decaying turbulence has been known to be heavily influenced by persisting coherent vortices that tend to steepen the shape of the energy spectra. The wavelet expansion of the denoised data has led us to reasonable extraction of coherent structures from stochastic fluctuations that belong to filamentary distributions. The stochastic component is confirmed to have the energy spectrum following the power law $E(k) \propto k^{-\alpha}$ with the index of $\alpha \approx 3$ as expected in the theoretical model of the two-dimensional turbulence.

These results were not obtained without the wavelet analysis that preserves local information of spatial structure at each scale, and demonstrate the usefulness of this analysis to extract uncultivated aspects of magnetized pure electron plasmas as an ideal test bench for investigating Euler fluid dynamics.

**ACKNOWLEDGMENTS**

The authors greatly appreciate Professor Y. Kaneda of Nagoya University for inspiring the usefulness of the wavelets to the correlational analysis of vortex dynamics and turbulence. We also acknowledge collaboration with Dr. Y. Soga and Dr. J. Aoki in starting the experimental studies of the vortex dynamics in turbulence. This work was supported by the Grant-in-Aid program of JSPS and partly by the collaborative research program of NIFS.

[1] C. F. Driscoll and K. S. Fine, Phys. Fluids B **2**, 1359 (1990).
[2] T. B. Mitchell and C. F. Driscoll, Phys. Fluids **8**, 1828 (1996).
[3] K. S. Fine, A. C. Cass, W. G. Flynn, and C. F. Driscoll, Phys. Rev. Lett. **75**, 3277 (1995).
[4] A. J. Peurrung and J. Fajans, Phys. Fluids A **5**, 493 (1993).
[5] Y. Kiwamoto, N. Hashizume, Y. Soga, J. Aoki, and Y. Kawai, Phys. Rev. Lett. **99**, 115002 (2007).
[6] Y. Kawai, Y. Kiwamoto, K. Ito, A. Sanpei, Y. Soga, J. Aoki, and K. Itoh, J. Phys. Soc. Jpn. **75**, 104502 (2006).
[7] Y. Kawai, Y. Kiwamoto, Y. Soga, and J. Aoki, Phys. Rev. E **75**, 066404 (2007).
[8] R. H. Kraichnan, Phys. Fluids **10**, 1417 (1967).
[9] G. K. Batchelor, Phys. Fluids **12** (Suppl. II), 233 (1969).
[10] U. Frisch, *Turbulence* (Cambridge University Press, Cambridge, UK, 1995), p. 241.
[11] M. Farge, Annu. Rev. Fluid Mech. **24**, 395 (1992).
[12] V. Perrier, T. Philipovitch, and C. Basdevant, J. Math. Phys. **36**, 1506 (1995).
[13] I. Daubechies, *Ten Lectures on Wavelets* (SIAM, Philadelphia, 1992).
[14] Y. Kiwamoto, K. Ito, A. Sanpei, and A. Mohri, Phys. Rev. Lett. **85**, 3173 (2000).
[15] K. Ito, Y. Kiwamoto, and A. Sanpei, Jpn. J. Appl. Phys., Part 1 **40**, 2558 (2001).
[16] J. Aoki, Y. Kiwamoto, Y. Soga, and A. Sanpei, Jpn. J. Appl. Phys., Part 1 **43**, 7267 (2004).
[17] D. Donoho and I. Johnstone, Biometrika **81**, 425 (1994).
[18] M. Farge, K. Schneider, and N. Kevlahan, Phys. Fluids **11**, 2187 (1999).
[19] D. H. E. Dubin and T. M. O'Neil, Phys. Plasmas **5**, 1305 (1998).
[20] M. Do-Khac, C. Basdevant, V. Perrier, and K. Dang-Tran, Physica D **76**, 252 (1994).
[21] K. Schneider, M. Farge, and N. Kevlahan, in *Woods Hole Mathematics, Perspectives in Mathematics and Physics*, edited by N. Tongring and R. C. Penner (World Scientific, Singapore, 2004), Vol. 34, p. 302.
[22] N. Okamoto, K. Yoshimatsu, K. Schneider, M. Farge, and Y. Kaneda, Phys. Fluids **19**, 115109 (2007).
[23] See U. Frisch, *Turbulence* Ref. [10], p. 120.
[24] P. Tabeling, Phys. Rep. **362**, 1 (2002).
[25] J. C. McWilliams, J. Fluid Mech. **146**, 21 (1984).
[26] P. Santangelo, R. Benzi, and B. Legras, Phys. Fluids A **1**, 1027 (1989).
[27] N. K.-R. Kevlahan and M. Farge, J. Fluid Mech. **346**, 49 (1997).
[28] P. G. Saffman, Stud. Appl. Math. **50**, 377 (1971).
[29] A. D. Gilbert, J. Fluid Mech. **193**, 475 (1988).